

## Supporting Information

for *Laser Photonics Rev.*, DOI 10.1002/lpor.202300217

Programmable Aperture Light-Field Microscopy

*Zewei Cai, Runnan Zhang, Ning Zhou, Qian Chen\* and Chao Zuo\**

## Supporting Information

# Programmable Aperture Light-Field Microscopy

*Zewei Cai, Runnan Zhang, Ning Zhou, Qian Chen,\* and Chao Zuo\**

## Abstract

This document provides supplementary information to “Programmable aperture light field microscopy”.

## Contents

- S1. Microscopic imaging model**
- S2. Incoherent Fourier slice theorem for PALFM**
- S3. Reconstruction algorithms for PALFM**
- S4. Hybrid aperture modulation scheme**
- S5. Effect of SLM structure on aperture modulation**
- S6. Standard image of resolution target**
- S7. Imaging performance of PALFM with centrosymmetric apertures**
- S8. PALFM volumetric imaging with different wavelengths**
- S9. PALFM volumetric imaging with different aperture parameters**
- S10. Histology image of mouse kidney section**
- S11. OTF analysis of PALFM**

## S1. Microscopic imaging model

The imaging process of a coherent diffraction-limited system can be represented as the convolution of the object wavefield and the impulse response, namely the amplitude point spread function (APSF) denoted as  $h(\mathbf{x})$ , where  $\mathbf{x} = (x, y)^T$  is the transverse spatial coordinates. The Fourier transform of APSF is the coherence transfer function (CTF):  $\mathcal{H}(\kappa_x) = \mathcal{F}_x[h(\mathbf{x})]$ , where  $\mathcal{F}_x[\cdot]$  denotes the Fourier transform with respect to  $\mathbf{x}$ , and  $\kappa_x = (\kappa_x, \kappa_y)^T$  is the transverse spatial frequency coordinates. The CTF corresponds to the pupil of the imaging system on the focal plane. For object points on out-of-focus planes, the defocused CTF (DCTF) by adding a propagation factor toward the focal plane can be used<sup>[1]</sup>

$$\mathcal{H}(\kappa_x, z) = \mathcal{H}(\kappa_x) \mathcal{D}(z) = \mathcal{H}(\kappa_x) e^{i2\pi z \sqrt{\kappa^2 - |\kappa_x|^2}} \quad (\text{S1})$$

where  $\mathcal{D}(z)$  denotes the phase term introduced by a propagation distance of  $z$ ,  $\kappa = 1/\lambda$  is the wave number, and  $\lambda$  is the wavelength. The DCTF is generally regarded as the generalized pupil of the imaging system. By Fourier transforming the DCTF with respect to  $z$ , the three-dimensional CTF (3D-CTF) can be obtained such that

$$\mathcal{H}(\kappa_x, \kappa_z) = \mathcal{F}_z[\mathcal{H}(\kappa_x, z)] = \mathcal{H}(\kappa_x) \delta\left(\kappa_z - \sqrt{\kappa^2 - |\kappa_x|^2}\right) \quad (\text{S2})$$

where  $\kappa_z$  is the axial spatial frequency coordinate and  $\delta(\cdot)$  denotes the Dirac function. Geometrically, Equation S2 represents the projection of the two-dimensional pupil onto a 3D spherical shell.

For an incoherent imaging system, the imaging process is characterized by the optical transfer function (OTF) and intensity PSF (IPSF), namely the modulus square of APSF, which satisfies the following relationship:

$$\begin{aligned} H(\kappa_x, \kappa_z) &= \mathcal{F}_z[H(\kappa_x, z)] = \mathcal{F}_{\mathbf{x}, z} \left[ |h(\mathbf{x}, z)|^2 \right] \\ &= \mathcal{H}(\kappa_x, \kappa_z) \star_{\kappa_x, \kappa_z} \mathcal{H}(\kappa_x, \kappa_z) \end{aligned} \quad (\text{S3})$$

where  $\star$  is the correlation operator,  $H(\kappa_x, z)$  denotes the defocused OTF (DOTF), and  $H(\kappa_x, \kappa_z)$  denotes the 3D-OTF, which is equal to the 3D autocorrelation of 3D-CTF. Accordingly, the DOTF is equivalent to the autocorrelation of DCTF with respect to  $\kappa_x$ , and satisfies the following basic properties:

- (1) The DOTF is Hermitian, i.e.,  $H(\kappa_x, z) = H^*(-\kappa_x, z)$ .
- (2) If the pupil is real, then  $H(\kappa_x, z) = H^*(\kappa_x, -z)$ .
- (3) If the pupil is symmetrical about the center, then  $H(\kappa_x, z) = H(-\kappa_x, z)$ .

The analytical expression of the 3D-APSF can be established through the scalar (for low numerical aperture objectives) or vector (for high numerical aperture objectives) Debye theory. Alternatively, one can establish the function of CTF to compute the 3D-OTF using Equation S2 and S3. The CTF corresponding to an objective lens with a circular aperture can be formulated as  $\mathcal{H}(\kappa_x) = \mathcal{P}(\alpha) / \sqrt{\kappa^2 - |\kappa_x|^2}$ , where  $\alpha$  is the semi-aperture angle, satisfying  $\sin \alpha = |\kappa_x| / \kappa$ , and  $\mathcal{P}(\alpha)$  denotes the apodization function, represented as  $\mathcal{P}(\alpha) = \sqrt{\cos \alpha}$  under the Abbe sine condition.

According to the above definition, the incoherent forward imaging model on the focal plane for wide-field microscopy can be expressed as  $i(\mathbf{x}) = \left[ |h(\mathbf{x}, z)|^2 \otimes_{\mathbf{x}, z} o(\mathbf{x}, z) \right]_{z=0}$ , where  $i(\mathbf{x})$  and  $o(\mathbf{x}, z)$  denote the image and 3D object, respectively. Based on the convolution property, the forward imaging model can further be transformed into:

$$I(\kappa_x) = \int H(\kappa_x, -z) \cdot O(\kappa_x, z) dz = \int H(\kappa_x, \kappa_z) \cdot O(\kappa_x, \kappa_z) d\kappa_z \quad (\text{S4})$$

where  $I(\kappa_x)$  and  $O(\kappa_x, \kappa_z)$  denote the image spectrum and 3D object spectrum, respectively. Equation S4 reveals that wide-field microscopic imaging involves a projection process, either a spatial convolution projection or a frequency filtering projection.

## S2. Incoherent Fourier slice theorem for PALFM

In this section, we make a derivation for the incoherent Fourier slice theorem using annular apertures, which is the core mechanism of tomographic reconstruction for PALFM volumetric imaging. For the sake of concision, the constant components that do not impact the conclusion will be neglected. When a circular aperture is used in the imaging system, the 3D-APSF can be represented as<sup>[2]</sup>

$$h(v, u) = \int_0^1 P(\rho) e^{i \frac{u}{2} \rho^2} J_0(v \rho) \rho d\rho \quad (S5)$$

where  $v = 2\pi r a / \lambda d$  and  $u = 2\pi z a^2 / \lambda d^2$  are the axial and transverse optical coordinates, respectively,  $P(\rho)$  denotes the pupil function with the normalized radial coordinate  $\rho = r/a$ ,  $r = |\mathbf{x}|$  is the radial coordinate of the pupil,  $d$  is the distance from the pupil to the focal plane, and  $J_i$  denotes the first-kind Bessel function of order  $i$ .

If the circular aperture is obstructed to be an annular aperture with an inner radius  $\varepsilon a$ , the pupil function satisfies  $P(\rho) = 1, 0 \leq \rho \leq 1$ , where  $\varepsilon$  is the obstruction ratio. When an object point is imaged with the annular aperture, the light intensity in the axial image and along the axis are given respectively by<sup>[3]</sup>

$$i(v) = |h(v, u=0)|^2 = \left[ \frac{2J_1(v)}{v} - \frac{2\varepsilon J_1(\varepsilon v)}{v} \right]^2 \quad (S6)$$

$$i(u) = |h(v=0, u)|^2 = \left[ \frac{\sin\left[u/4(1-\varepsilon^2)\right]}{u/4} \right]^2 \quad (S7)$$

Equation S6 can be simplified to  $[2J_1(v)/v]^2$  and  $J_0^2(v)$  for an unobstructed circular aperture ( $\varepsilon = 0$ ) and an infinitesimal width annular aperture ( $\varepsilon \rightarrow 1$ ), respectively. The latter produces an Airy pattern with a smaller FWHM (full width at half maximum) than the former, indicating that the spatial resolution can be improved to some extent by using annular apertures. On the other hand, it can be seen from Equation S7 that the defocus distance at which  $i(u)$  drops to a certain value is increased by a factor  $1/(1-\varepsilon^2)$ , resulting in a larger depth-of-field when using annular apertures. Especially, from Equation S5 the 3D-IPSF of the infinitesimal width annular aperture can be deduced to be<sup>[4]</sup>

$$|h(v, u)|_{\varepsilon \rightarrow 1}^2 = J_0^2(v) \quad (S8)$$

Equation S8 reveals an essential phenomenon that with such an annular aperture the PSF of the incoherent imaging system keeps constant axially, regardless of the propagation distance. It implies that incident light fields can be manipulated to be diffraction-free Bessel-like beams in the Fourier

space through back-end aperture modulation. While the PSF patterns produced by circular apertures quickly spread in the axial image during light propagation, using annular apertures maintains the strip-shaped 3D-PSF across a large depth range. Images formed via the diffraction-free 3D-IPSF are equivalent to the projection of 3D observed samples along the line direction. If we change the annular aperture with different rotation angles around the optical axis, the strip-shaped 3D-PSFs turn to be ones with different polar angles with respect to the  $z$  axis, resulting in various projections along different line directions. According to the projection slice theorem<sup>[5]</sup>, these projections in the spatial domain correspond to different slices in the frequency domain. That is the incoherent Fourier slice theorem built on aperture modulation for PALFM.

Alternatively, the incoherent Fourier slice theorem can be derived based on the OTF. The 3D-OTF related to an annular aperture can be represented as<sup>[6]</sup>

$$H(\kappa_r, \kappa_z) = \frac{1}{|\kappa_r|} \left\{ \text{Re} \left[ \sqrt{1 - \left( \frac{|\kappa_z|}{\kappa_r} + \frac{\kappa_r}{2} \right)^2} \right] - \text{Re} \left[ \sqrt{\varepsilon^2 - \left( \frac{|\kappa_z|}{\kappa_r} + \frac{\kappa_r}{2} \right)^2} \right] \right\} \quad (\text{S9})$$

where  $\kappa_r$  and  $\kappa_z$  are radial (*i.e.*,  $\kappa_r = |\kappa_x|$ ) and axial spatial frequency coordinates normalized by  $\sin \alpha / \lambda$  and  $4 \sin^2(\alpha/2) / \lambda$ , respectively, and  $\text{Re}[\cdot]$  denotes the real-value operation. The first term on the right-hand side of Equation S9 is related to the circular aperture when  $\varepsilon = 0$ , and in this case, the second term becomes zero. The transverse normalized cut-off frequency is 2, while the axial one becomes  $(1 - \varepsilon^2) / 2$ , which tends to zero when  $\varepsilon \rightarrow 1$ . Thus, the 3D-OTF of the annular aperture has non-zero values only on the plane of  $\kappa_z = 0$ . When the annular aperture is rotated around the optical axis, a similar plane-shaped 3D-OTF is formed with specific polar angles with respect to the  $\kappa_z$  axis and across the origin. Accordingly, we can formulate the 3D-OTF in Equation S3 to be

$$H_{\theta}(\kappa_x, \kappa_z) = H(\kappa_x, \kappa_z) \cdot \delta(\mathbf{a}_{\theta} \kappa_x - \kappa_z) \quad (\text{S10})$$

where  $\mathbf{a}_{\theta}$  is the plane normal vector corresponding to the polar angles  $\theta$ . Substituting Equation S10 to Equation S4, we can get

$$I_{\theta}(\kappa_x) = H(\kappa_x, \mathbf{a}_{\theta} \kappa_x) \cdot O(\kappa_x, \mathbf{a}_{\theta} \kappa_x) \quad (\text{S11})$$

That is the incoherent Fourier slice theorem for PALFM, which represents that the image spectrum is the projection of the object spectrum modulated by the plane-shape 3D-OTF corresponding to the annular aperture.

### S3. Reconstruction algorithms for PALFM

The incoherent Fourier slice theorem proposed indicates that PALFM can be regarded as a tomographic imaging modality suitable for incoherent microscopic imaging systems. Thus, tomographic reconstruction algorithms similar to traditional computed tomography<sup>[7]</sup> may be designed for PALFM volumetric imaging. When annular apertures are used for imaging, each image spectrum corresponds to a specific central slice of the 3D object spectrum modulated by the 3D-OTF and can be directly back-projected to the object spectrum, as illustrated in Figure 1b. As a result, the 3D object information can be recovered by collecting sufficient image spectrums to completely fill up the object spectrum. However, the filled object spectrum may not be uniform since every two slices have an interaction line.

Alternatively, when considering frequency coverage and thus using the designed hybrid aperture modulation scheme consisting of not only annular but also circular apertures, the direct back-projection algorithm may fail due to the inapplicability of the incoherent Fourier slice theorem for circular apertures (see Figure 1e). Let us call back the forward imaging model in Equation S4. The image spectrum is equal to the projection of the modulated object spectrum with respect to the  $z$  axis. The DOTF of the respective aperture provides a specific spatial frequency constraint for each object layer. This implies that the image spectrum can be optimally “back-projected” to specific object layers when non-centrosymmetric apertures are used for non-ambiguous depth discrimination. Here, the reconstruction algorithm aims at recovering the object layer sequence  $\{o(\mathbf{x}, z_n)\}$  from the image sequence  $\{i_m(\mathbf{x})\}$ . Accordingly, we design a non-linear iterative reconstruction algorithm for PALFM volumetric imaging with the aperture modulation scheme of non-centrosymmetric annular and circular apertures, involving the following steps (see also the flow chart in Figure S1):

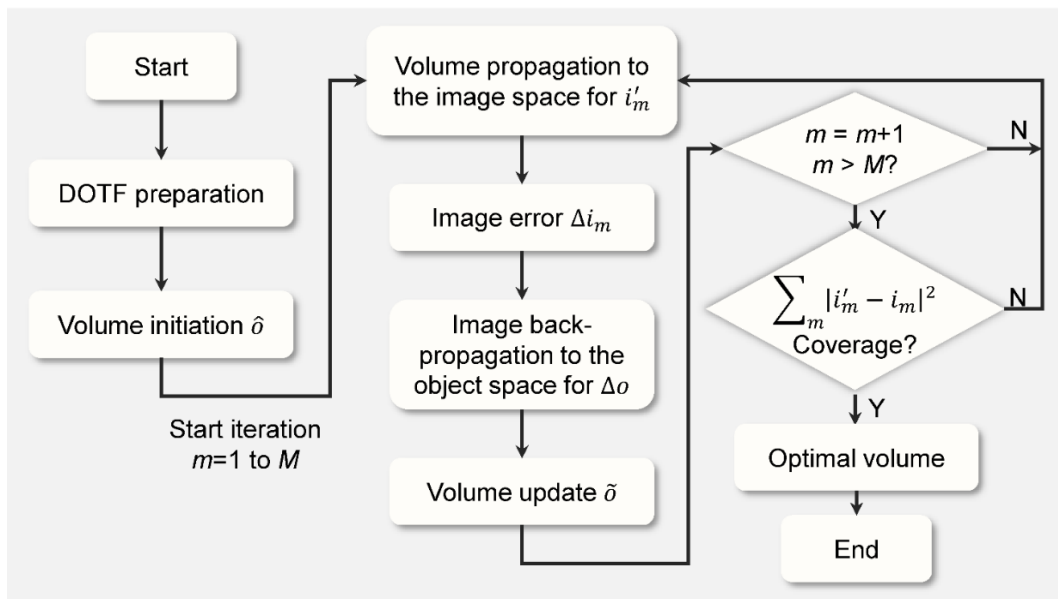


**Figure S1.** Flow chart iterative optimization algorithm for PALFM tomographic reconstruction.

**Step 1.** The DOTF related to each aperture is prepared by theoretically calculating with known system parameters or experimentally calibrating in advance.

**Step 2.** The volume is initially estimated through a linear solution that

$$\hat{o}(\mathbf{x}, z_n) = \mathcal{F}_x^{-1} \left[ \frac{\sum_m H_m^*(\kappa_x, z_n) \cdot I_m(\kappa_x)}{\sum_m |H_m(\kappa_x, z_n)|^2 + \beta} \right] \quad (\text{S12})$$

where  $\beta$  is the regularization factor. The linear solution implicitly assumes that the image information or energy is equally distributed to each object layer during backward projection.

**Step 3.** By starting from the first coded aperture, the volume is propagated to the image space to obtain the computed image through the forward imaging model and the corresponding DOTF (Equation S4). The computed image is compared with the detected image to correspondingly obtain the image error term.

**Step 4.** The image error term is back-propagated to each object layer to obtain the object error term (similar to Equation S12 in which the summation of the total apertures is replaced by the current aperture), and the volume is updated using this error term.

**Step 5.** After all coded apertures have already participated in updating the volume, the total residual can be obtained from the last updated volume. If the residual is greater than a user-defined threshold, the volume will be re-updated from the first coded aperture. If the residual converges to the threshold, the entire 3D reconstruction is completed, resulting in the final optimal volume.



#### **S4. Hybrid aperture modulation scheme**

The designed hybrid aperture modulation scheme contained 6 annular and 6 circular aperture sequences, as shown by schematic diagrams in detail in Figure S2 and S3, respectively. The normalized diameter for each aperture sequence was changed from 0.5 to 1 with a step of 0.1. The number of apertures in each sequence was set to 8, 7, 5, 4, 2, and 1, respectively. The annular aperture width was 0.05 times the radius of the full aperture. Considering that apertures with different unobstructed regions have different photon efficiencies, different exposure periods were set up for annular and circular apertures, e.g., 30 ms and 15 ms, respectively. Thus, the hybrid aperture modulation scheme included 27 annular and 27 circular apertures and had ~1 Hz volumetric imaging speed.

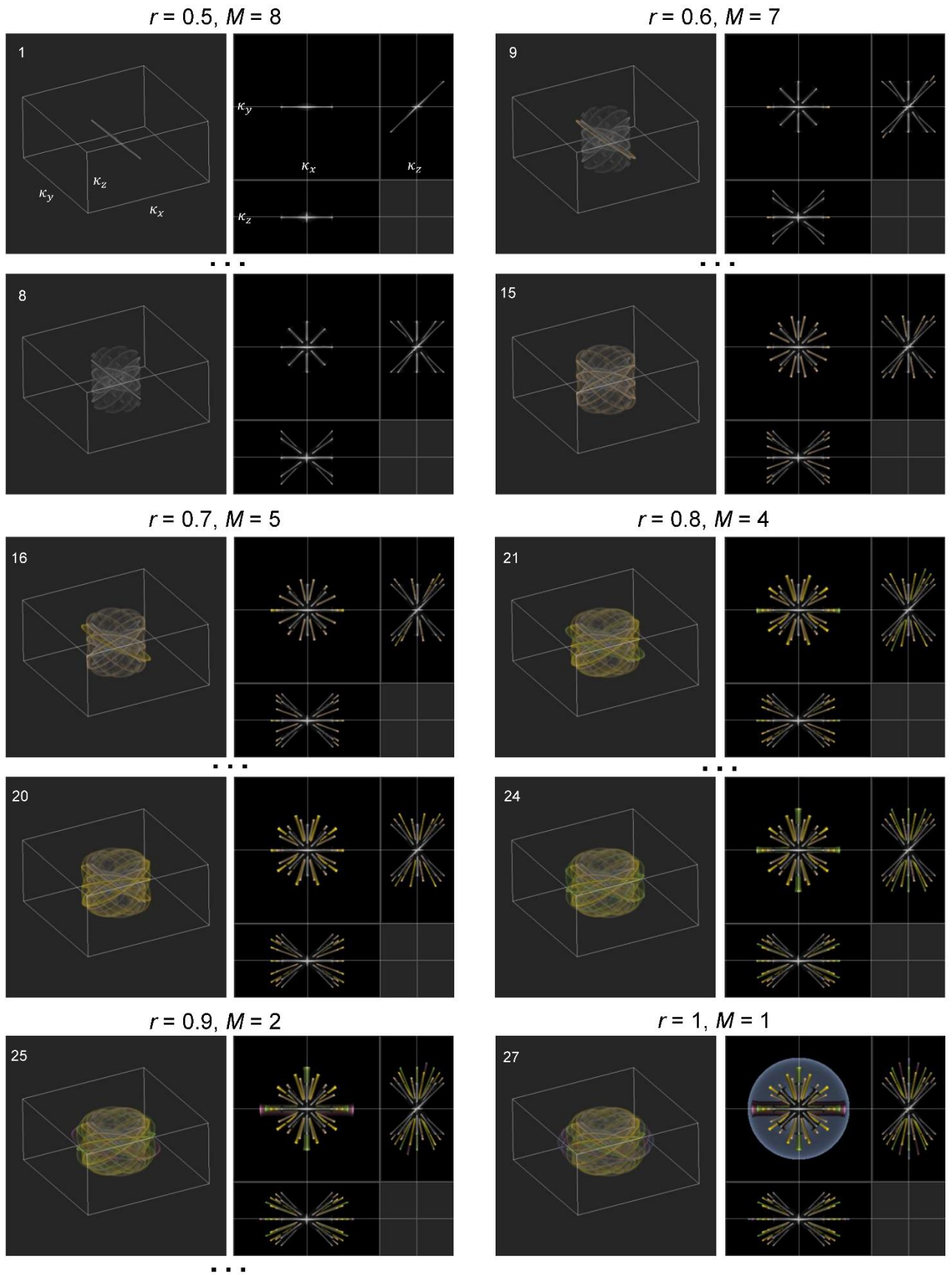


**Figure S2.** 3D-OTF distributions, along with spectral cross-sections along each axis, corresponding to different annular aperture sequences with different diameters and rotated angles.

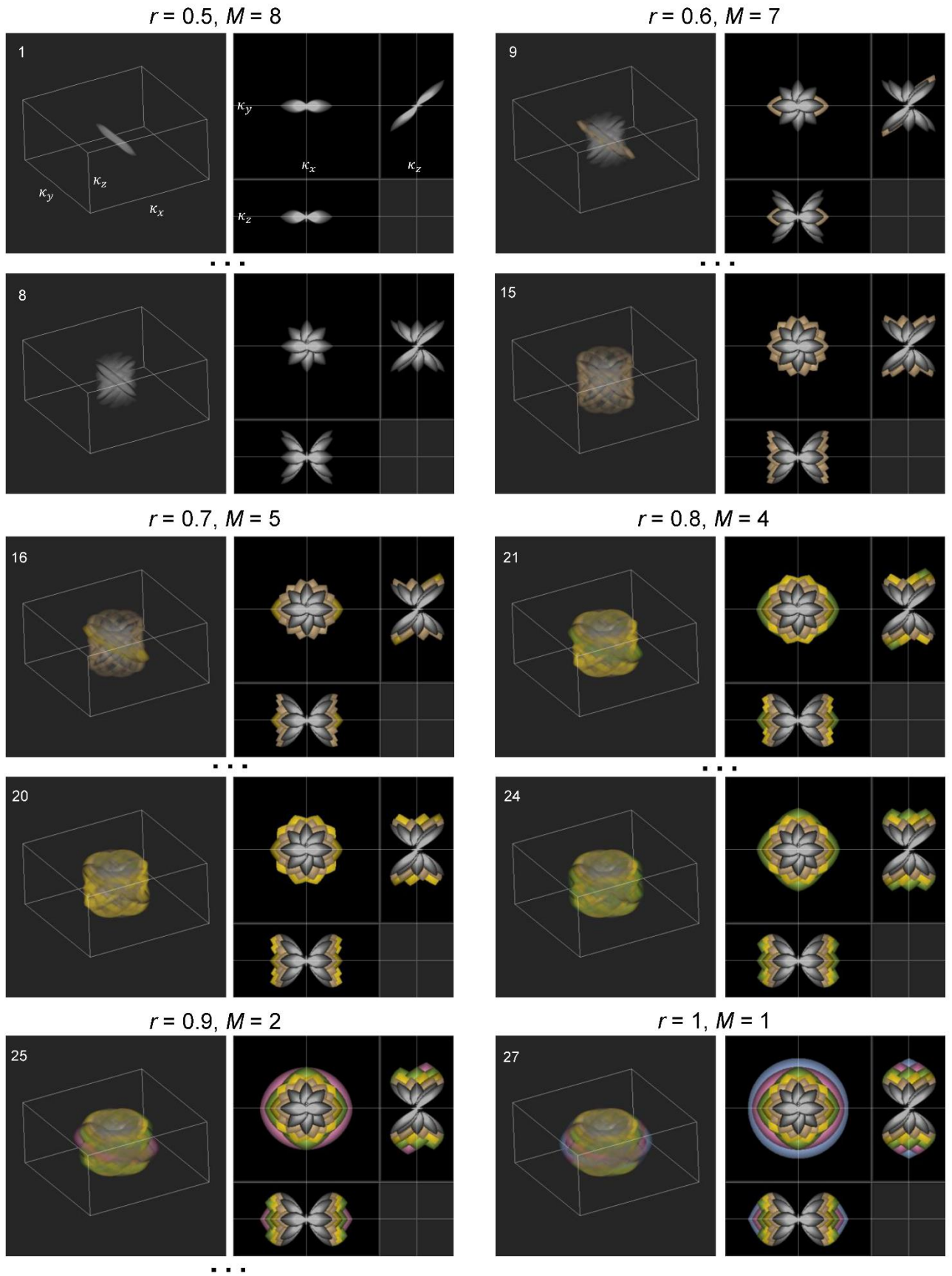


**Figure S3.** 3D-OTF distributions, along with spectral cross-sections along each axis, corresponding to different circular aperture sequences with different diameters and rotated angles.

## S5. Effect of SLM structure on aperture modulation

The SLM used in the programmable aperture module is a digital device. Thus, pixel quantization may have a prominent effect on aperture modulation. Especially for annular apertures, their widths are required to be as small as possible in order to satisfy the incoherent Fourier slice theorem. However, due to the pixel quantization of the SLM, the annular aperture width will not be lower than one-pixel size, which may cause discontinuous light-field modulation, as illustrated by white arrows in Figure S4a. It may eventually introduce calculation errors to the volumetric reconstruction. In this work, the designed hybrid aperture modulation scheme can relax the restriction on the annular aperture width, which is set to be 0.05 times the radius of the full aperture. If the 4f relay system is adjusted to make the size of the equivalent pupil on the SLM surface  $2/3$  of the size of the SLM, the annular aperture width occupies about 18 pixels. Figure S4b diagrammatically shows this experimental case, in which the effect of SLM pixel quantization can be somewhat ignored.

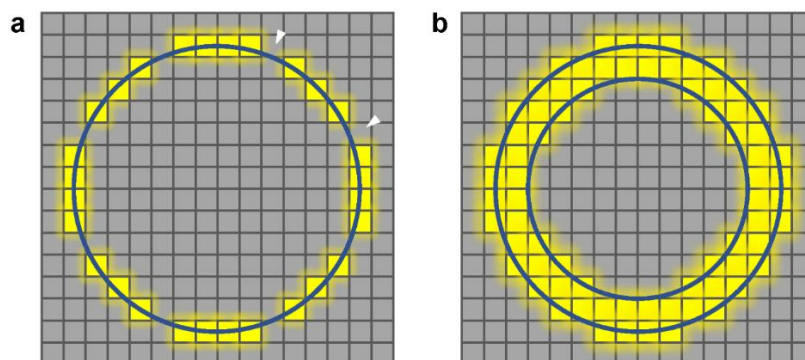


**Figure S4.** Effect of SLM structure on aperture modulation. Annular apertures with a (a) small and (b) large width.

## S6. Standard image of resolution target

The standard image of the USAF-1951 resolution target used in the experiment is shown in Figure S5. The labeling numbers of different groups and elements on the resolution target can be recognized from imaging results to reflect the resolution capability of the imaging system and method.

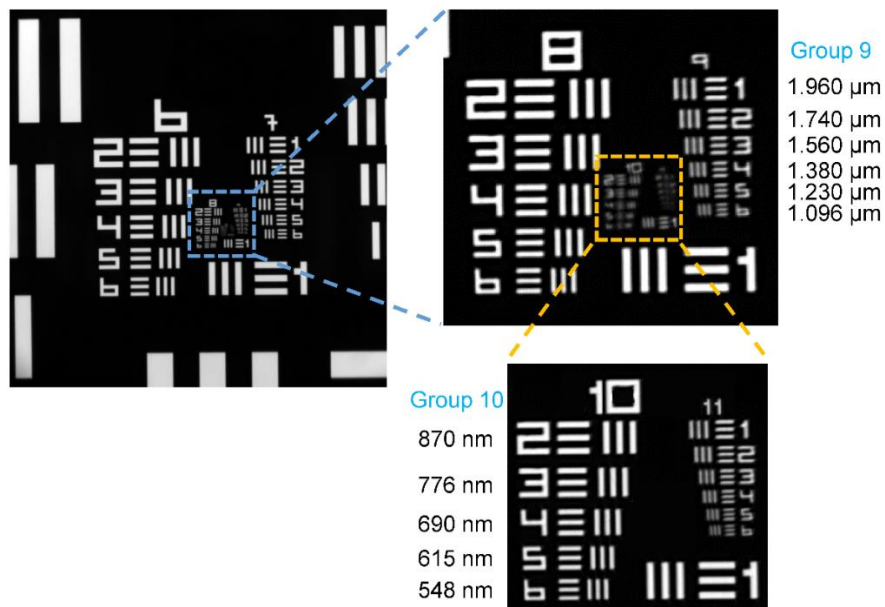


**Figure S5.** Standard image of the USAF-1951 resolution target.

## S7. Imaging performance of PALFM with centrosymmetric apertures

The aperture modulation enables PALFM to recover the 3D object spectrum from the image spectrums. Here, we made a simulation to demonstrate and analyze the imaging performance of PALFM. The system parameters were the same as those in the experiment related to Figure 2. An obliquely placed resolution target within a depth range of  $\pm 50 \mu\text{m}$  was used as an observed sample, as shown by the maximum intensity projection (MIP) along each axis in Figure S6a. Figure S6b shows the image of the resolution target under the full aperture. At first, we used a non-centrosymmetric circular aperture sequence with the same diameter as half of the full aperture and different rotation angles around the optical axis to perform PALFM volumetric imaging. Figure S6c shows images of the resolution target under the circular apertures with different rotation angles. The final reconstruction result is visualized by the MIP in Figure S6d. It can be seen that the reconstructed volume can reflect the whole spatial distribution trend of the observed sample but cannot resolve the details very well. Since the observed sample is modulated by the OTF, the recovered object spectrum from the image spectrums is limited by the cut-off frequency of the diffraction-limited imaging system such that

$$\hat{O}(\kappa_x, \kappa_z) \simeq O(\kappa_x, \kappa_z) \Big|_{\mathbb{R}_{\kappa_x, \kappa_z} \{H(\kappa_x, \kappa_z)\}} \quad (\text{S13})$$

Thus, the object spectrum beyond the cut-off frequency of the half-diameter apertures cannot be effectively transmitted and recovered.

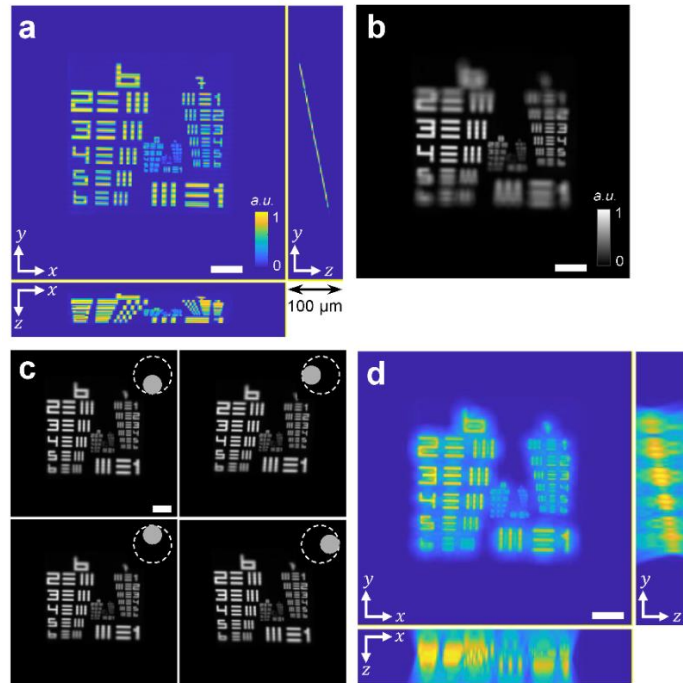


**Figure S6.** PALFM simulation. (a) MIP of the obliquely placed resolution target; (b) image of the resolution target under the full aperture; (c) images of the resolution target under the circular aperture with different rotation angles and (d) MIP of the reconstructed volume. Scale bar, 50  $\mu\text{m}$ .



Next, we used two kinds of coded apertures with sizes comparable to the full aperture to perform PALFM volumetric imaging. The first example used two equal-sized, side-by-side circles to form a double-circle aperture pattern, whose 3D-OTF distribution and spectral cross-sections along each axis are shown in Figure S7a. Similarly, the double-circle aperture was rotated around the optical axis, and images were obtained correspondingly, as shown in Figure S7b. Figure S7c shows the MIP of the reconstructed volume. The comparison with the result in Figure S6d indicates that the double-circle aperture sequence cannot recover the correct spatial distribution trend of the observed sample. Another example was an elliptical aperture pattern with a long axis equal to the diameter of the full aperture. Figure S7d shows the 3D-OTF distribution of the elliptical aperture and its spectral cross-sections along each axis. Images formed by rotating the elliptical aperture and the final reconstruction result are shown in Figure S7e and S7f, respectively. As with the double-circle aperture, the elliptical aperture also failed to demodulate non-ambiguous depth information of the observed sample, although their 3D-OTFs can reach the cut-off frequency of the full aperture.

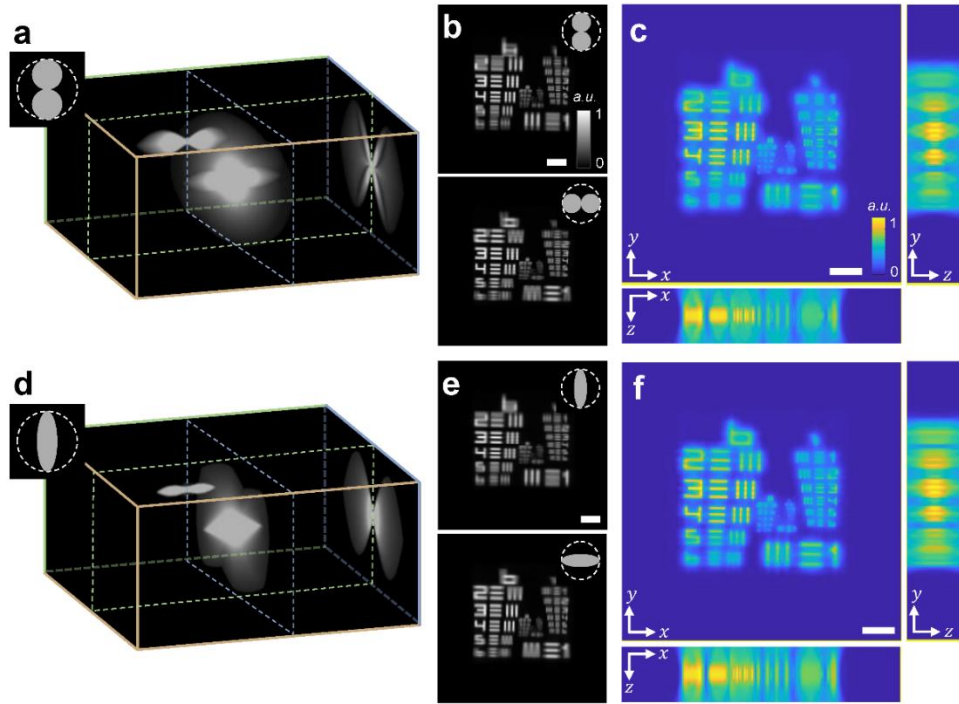


**Figure S7.** PALFM volumetric imaging using centrosymmetric apertures. (a) 3D-OTF distribution of the double-circle aperture; (b) images of the resolution target under the double-circle aperture with different rotation angles and (c) MIP of the reconstructed volume; (d) 3D-OTF distribution of the elliptical aperture; (e) images of the resolution target under the elliptical aperture with different rotation angles and (f) MIP of the reconstructed volume. Scale bar, 50  $\mu\text{m}$ .

By observing Figure S7c and S7f, it can be found that the MIPs of the reconstructed volumes along the  $x$  and  $y$  axes are both symmetrical about the  $z$  axis. This is intrinsically related to the imaging properties of the chosen coded aperture patterns. When a centrosymmetric aperture is used, the

imaging system simultaneously satisfies properties (1) – (3). Consequently, the DOTF satisfies  $H(\kappa_x, z) = H(\kappa_x, -z)$ , making the 3D-OTF be  $H(\kappa_x, \kappa_z) = H(\kappa_x, -\kappa_z)$ . That is, the 3D-OTF is symmetric about the  $\kappa_z$  axis, as illustrated by the spectral cross-sections in Figure S7a and S7d. In this situation, an opposite object spectrum  $O(\kappa_x, -\kappa_z)$  will produce the same image spectrum as the original object spectrum, causing the ambiguity problem of depth discrimination. To avoid this issue, one can use non-centrosymmetric apertures for PALFM volumetric imaging.



## S8. PALFM volumetric imaging with different wavelengths

The 3D-OTF is a function of wavelength (see Section S1). Since PALFM achieves volumetric imaging through modulating aperture-related 3D-OTFs, different illumination/excitation wavelengths may result in different imaging performances. In this section, the obliquely placed resolution target as a reference sample (see Figure S6a) and the circular aperture sequence were used to illustrate how imaging performance changes with the wavelength. The resolution target was imaged respectively under three light beams as same as the experiment of multi-color PALFM volumetric imaging related to Figure 3. Since the size of the equivalent pupil in the Fourier plane changed with the wavelength, the size of coded apertures was correspondingly adjusted in each color channel according to the wavelength used, while the shape and number of coded apertures remained unchanged. The reconstruction results are shown in Figure S8a – S8c, which look almost indistinguishable. Figure S8d plots the local profiles of the reconstructed volumes related to the white line marked in Figure S8a. It can be seen that the spatial position of reconstructed voxels remains consistent regardless of wavelengths. Therefore, the spatial position registration in different color channels is unnecessary once the volume is accurately reconstructed from the detected image spectrums. On the other hand, the wavelength, together with the numerical aperture of the objective lens, determines the frequency range of the 3D-OTF. Thus, the object spectrum is recovered within different cut-off frequencies related to various wavelengths, resulting in different spatial resolutions, as shown by the profile indicated by the black arrow in Figure S8d.

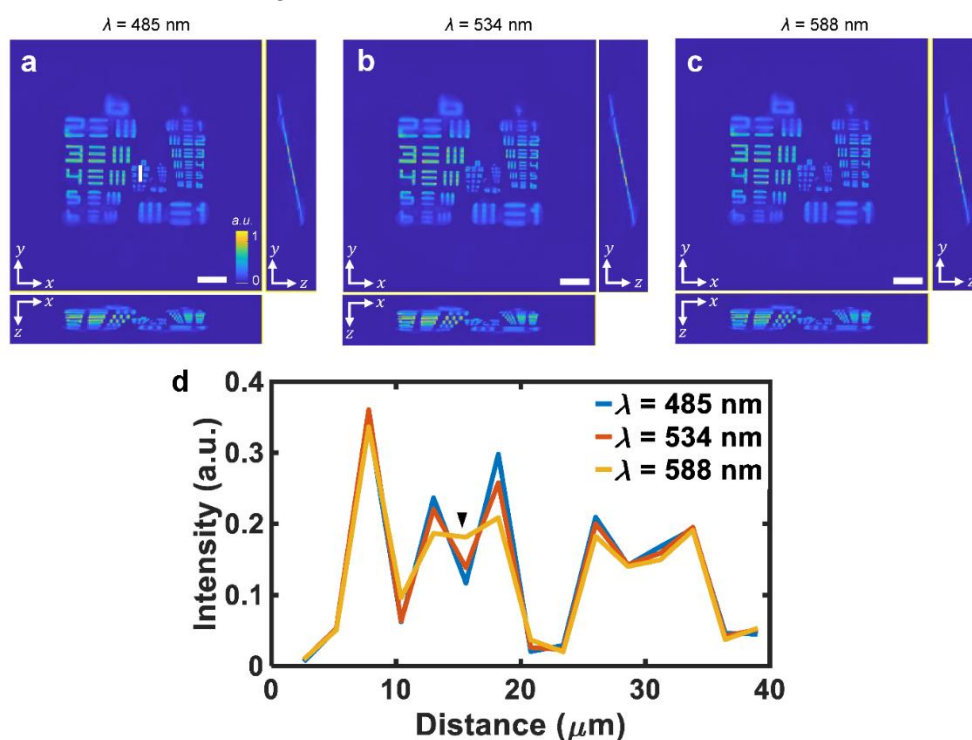


**Figure S8.** PALFM volumetric imaging with different wavelengths. (a) – (c) MIPs of the reconstructed volumes using three wavelengths; (d) line profiles related to the white line marked in (a). Scale bar, 50  $\mu\text{m}$ .

## **S9. PALFM volumetric imaging with different aperture parameters**

The effect of the shape and number of aperture modulation on the imaging performance of PALFM were considered and compared. The experimental condition was the same as that in Figure 3. A *Rhizopus nigricans* section was used as the observed sample. First, PALFM volumetric imaging using the hybrid aperture modulation scheme containing both annular and circular apertures was compared with that using the circular aperture sequence. Then, the number of apertures in the hybrid scheme was reduced by nearly half to perform PALFM tomographic reconstruction again for further comparison. Figure S9a – S9c show the MIPs of the three reconstructed volumes along each axis, corresponding to the hybrid aperture modulation scheme, the circular aperture sequence, and the hybrid scheme with fewer apertures, respectively. The comparison among the projections along the *x* and *y* axes shows that the reconstruction result concerning the hybrid aperture modulation scheme with more apertures can resolve more object details (see white arrows).

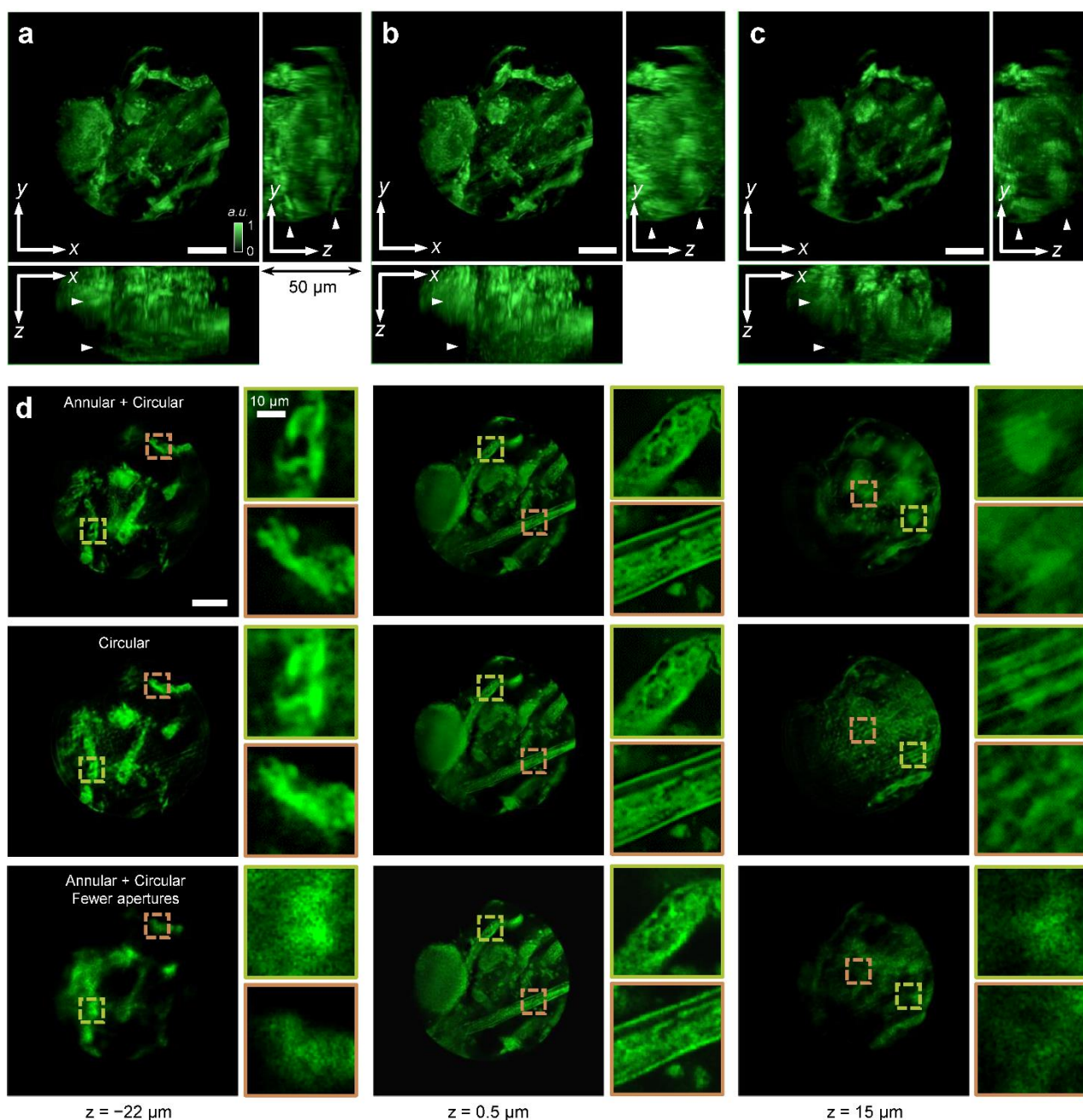


**Figure S9.** Comparison results of PALFM volumetric imaging of *Rhizopus nigricans* section. MIPs of the reconstructed volumes concerning (a) the hybrid aperture modulation scheme, (b) the circular aperture sequence, and (c) the hybrid scheme with fewer apertures; (d) object layer distributions of the reconstructed volumes at different axial positions along with enlarged local views. Scale bar, 50  $\mu\text{m}$ .

Figure S9d shows different object layer distributions and their enlarged local views at different axial positions for detailed comparison. Near the focal plane (see the second column in Figure S9d), the results in the three cases are almost identical. In contrast, at axial positions far away from the focal plane (see the first and third columns in Figure S9d), PALFM volumetric imaging using the hybrid aperture modulation scheme with more apertures exhibits the best resolution capacity. For the circular aperture sequence, artifacts appeared in the reconstructed volume, especially in the third column,

where the object structure could no longer be distinguished. The hybrid aperture modulation scheme with fewer apertures obtained the worst reconstruction result. The reason may be that the 3D-OTFs related to this scheme did not cover the whole object spectrum when the number of apertures was reduced, making the tomographic reconstruction sensitive to artifacts and noise.

The comparison result demonstrates that the imaging performance of PALFM changes with aperture parameters. The shape, size, number, and dimensionality of aperture modulation can be further investigated and optimized to design aperture modulation schemes with high-quality imaging performance. Here, we make a preliminary discussion on the shape and number of aperture modulation according to different experimental requirements. When the depth range of the observed sample is within the depth of field of circular apertures, it can be considered to use the circular aperture sequence for PALFM volumetric imaging because of the higher frequency coverage rate and photon efficiency. If the imaging depth range exceeds the depth of field of circular apertures, PALFM volumetric imaging can be performed by using the hybrid scheme containing both circular and annular apertures with an extended depth of field. In addition, if the sample has a high degree of discrimination, such as sparse point/depth-layer distribution, the number of coded apertures can be reduced to improve the volumetric imaging efficiency. Therefore, the number and shape of aperture modulation can be changed correspondingly according to specific experimental requirements, which may serve as a priori information.

## S10. Histology image of mouse kidney section

Figure S10 shows a conventional histology image which can be used to confirm the similar cellular structures of the mouse kidney section related to the experiment in Figure 3.

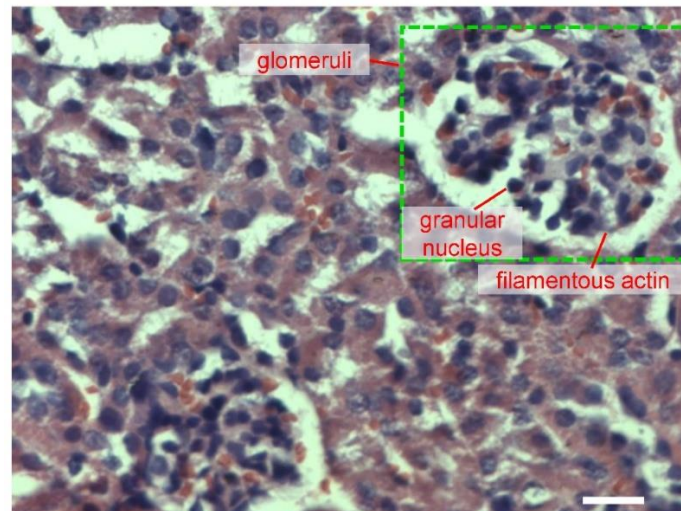


**Figure S10.** Histology image of mouse kidney section. Scale bar, 20  $\mu\text{m}$ .

## S11. OTF analysis of PALFM

The experiments of PALFM volumetric imaging show that different aperture sequences may result in various imaging performances. Here, the ability of PALFM to adjust the imaging performance is further analyzed by virtue of the OTF of the imaging system. Figure S11a plots the OTF distribution curves of the annular and circular apertures at different axial positions. Overall, the circular aperture has a better capability to transfer the object spectrum on the focal plane in the low and mid-frequency range, while this capability declines rapidly with increasing axial distance. In contrast, the annular aperture at first rapidly decays the OTF distribution to a low level and then keeps such a distribution trend mainly unchanged in the low and mid-frequency range, regardless of axial positions. The low-frequency region of the circular aperture oscillates and attenuates with spatial frequency, and the peak values rapidly decay below the OTF of the annular aperture when the axial position increases (see Arrow 1). In the high-frequency region, the annular aperture exhibits a remarkable characteristic that the OTF distribution jumps to a local maximum (see Arrow 2). In comparison, the OTF distribution of the circular aperture has already decayed to close to zero. In this case, the OTF of the annular aperture at 60  $\mu\text{m}$  axial position is already higher than that of the circular aperture at 20  $\mu\text{m}$  axial position (see Arrow 3).

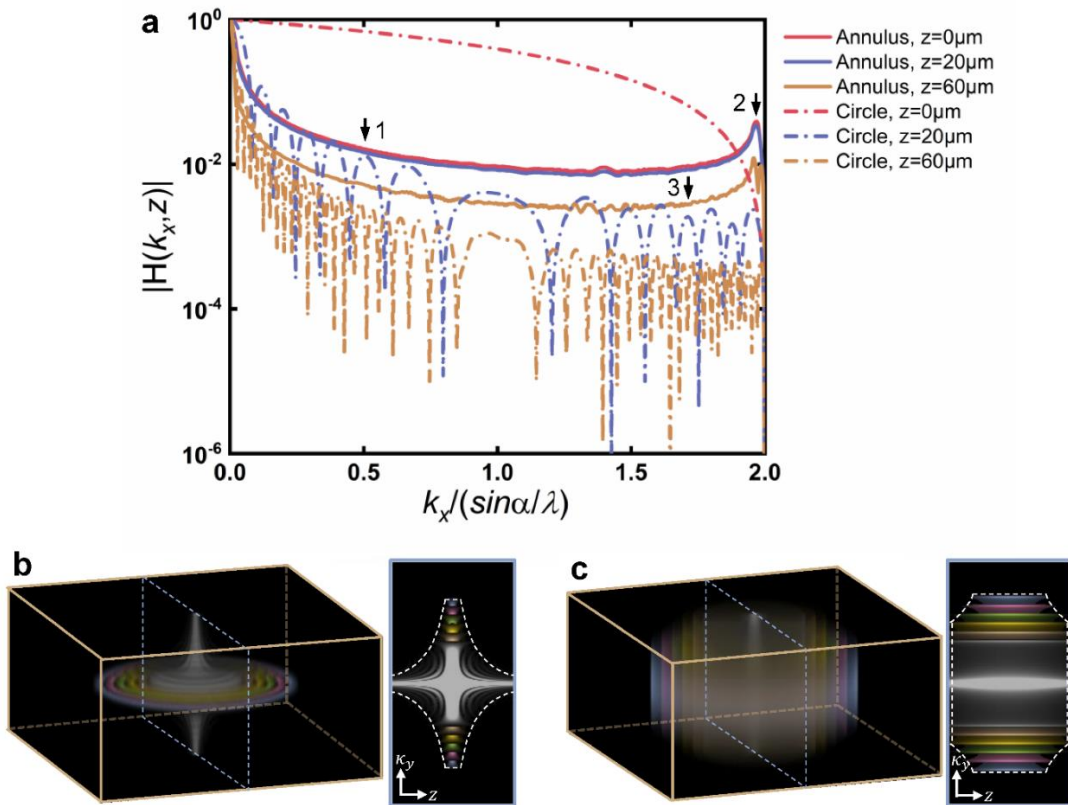


**Figure S11.** OTF analysis of PALFM. (a) OTF distribution curves of annular and circular apertures at different axial positions; DOTF distributions and their  $k_y - z$  slices of (b) circular and (c) annular apertures, related to Figure 1f and 1d, respectively.

Since the OTF is related only to the system parameters, the amplitude and frequency range of the OTF distribution determine the upper-limit ability of the imaging system to (de)modulate the 3D object spectrum. Figure S11b shows the DOTF distribution and its  $\kappa_y - z$  slice of the circular aperture sequence (related to Figure 1f). The white dashed outline illustrates the frequency range in which the object spectrum can be efficiently modulated. The circular aperture sequence can modulate the highest spatial frequency corresponding to the full aperture near the focal plane, but the efficient frequency range decreases rapidly with the increase of the axial distance. In other words, the spatial resolution decreases rapidly with increasing the imaging depth, which is consistent with the experimental results (see Figure 2e and 2f). In addition, the DOTF distribution of the circular aperture near the focal plane is relatively uniform, as shown by the gray region in the  $\kappa_y - z$  slice in Figure S11b. This indicates that the circular aperture has a high modulation ability for different object spectrum components in the cut-off frequency range near the focal plane.

Figure S11c shows the DOTF distribution and its  $\kappa_y - z$  slice of the annular aperture sequence (related to Figure 1d). Compared with the circular aperture, the annular aperture has two different properties. First, the annular aperture sequence can modulate the highest spatial frequency corresponding to the full aperture over a larger depth range. This is consistent with the imaging property of using the annular aperture to manipulate diffraction-free Bessel-like beams (see Equation S8). Thus, the annular aperture sequence maintains near-diffraction-limited spatial resolution and large depth-of-field simultaneously. Second, most of the energy of the optical signal modulated by the annular aperture is concentrated in the low-frequency region, while a small amount is in the high-frequency region. These two characteristics are mutually restrictive. When the width of the annular aperture gradually becomes smaller, the depth range in which the imaging system can effectively modulate the highest spatial frequency gradually expands. However, the photon efficiency and signal-to-noise ratio are correspondingly reduced with the decreased amount of passing light, which in turn affects the ability of object spectrum demodulation. In practical applications, the aperture modulation scheme can be designed by combining different kinds of coded aperture patterns, through which the low- and mid-frequency spectrum components in the depth range near the focal plane and the high-frequency spectrum components in a large depth range can be transmitted and modulated simultaneously, achieving superior imaging performance.

## Reference

- [1]. J. Mertz, *Introduction to Optical Microscopy*, Cambridge University Press **2019**.
- [2]. M. Gu, *Advanced Optical Imaging Theory*, Springer Science & Business Media **2000**.



- [3]. E. L. O'Neill, Transfer function for an annular aperture. *J. Opt. Soc. Am. A* **1956**, 46, 285.
- [4]. H. F. Tschunko, Imaging performance of annular apertures. *Appl. Opt.* **1974**, 13, 1820.
- [5]. D. H. Garces, W. T. Rhodes, N. M. Peña, Projection-slice theorem: a compact notation. *J. Opt. Soc. Am. A* **2011**, 28, 766.
- [6]. C. J. R. Sheppard, M. Gu, Three-dimensional optical transfer function for an annular lens. *Opt. Commun.* **1991**, 81, 276.
- [7]. A. C. Kak, M. Slaney, *Principles of computerized tomographic imaging*, SIAM **2001**.